



ARL-TR-7366 • Aug 2015



A Huygens Surface Approach to Antenna Implementation in Near-Field Radar Imaging System Simulations

by Traian Dogaru and DaHan Liao

Approved for public release; distribution unlimited.

NOTICES

Disclaimers

The findings in this report are not to be construed as an official Department of the Army position unless so designated by other authorized documents.

Citation of manufacturer's or trade names does not constitute an official endorsement or approval of the use thereof.

Destroy this report when it is no longer needed. Do not return it to the originator.



A Huygens Surface Approach to Antenna Implementation in Near-Field Radar Imaging System Simulations

by Traian Dogaru and DaHan Liao

Sensors and Electron Devices Directorate, ARL

REPORT DOCUMENTATION PAGE				Form Approved OMB No. 0704-0188	
<p>Public reporting burden for this collection of information is estimated to average 1 hour per response, including the time for reviewing instructions, searching existing data sources, gathering and maintaining the data needed, and completing and reviewing the collection information. Send comments regarding this burden estimate or any other aspect of this collection of information, including suggestions for reducing the burden, to Department of Defense, Washington Headquarters Services, Directorate for Information Operations and Reports (0704-0188), 1215 Jefferson Davis Highway, Suite 1204, Arlington, VA 22202-4302. Respondents should be aware that notwithstanding any other provision of law, no person shall be subject to any penalty for failing to comply with a collection of information if it does not display a currently valid OMB control number.</p> <p>PLEASE DO NOT RETURN YOUR FORM TO THE ABOVE ADDRESS.</p>					
1. REPORT DATE (DD-MM-YYYY)		2. REPORT TYPE		3. DATES COVERED (From - To)	
Aug 2015		Final		June 2014	
4. TITLE AND SUBTITLE A Huygens Surface Approach to Antenna Implementation in Near-Field Radar Imaging System Simulations				5a. CONTRACT NUMBER	
				5b. GRANT NUMBER	
				5c. PROGRAM ELEMENT NUMBER	
6. AUTHOR(S) Traian Dogaru and DaHan Liao				5d. PROJECT NUMBER R.0014706.20	
				5e. TASK NUMBER	
				5f. WORK UNIT NUMBER	
7. PERFORMING ORGANIZATION NAME(S) AND ADDRESS(ES) US Army Research Laboratory ATTN: RDRL-SER-U 2800 Power Mill Road Adelphi, MD 20783-1138				8. PERFORMING ORGANIZATION REPORT NUMBER ARL-TR-7366	
9. SPONSORING/MONITORING AGENCY NAME(S) AND ADDRESS(ES)				10. SPONSOR/MONITOR'S ACRONYM(S)	
				11. SPONSOR/MONITOR'S REPORT NUMBER(S)	
12. DISTRIBUTION/AVAILABILITY STATEMENT Approved for public release; distribution unlimited.					
13. SUPPLEMENTARY NOTES					
14. ABSTRACT This study introduces a new hybrid approach to implementing the radar transmitters and receivers in the NAFDTD simulation software, by replacing the physical antennas with equivalent currents sheets on a surrounding closed surface. After validating the code for several simple scenarios, we present a large-scale simulation in the presence of multiple targets embedded in a rough ground environment. The model consists of an ultra-wideband, forward-looking radar imaging system, equipped with a multi-static antenna array and mounted on a forward-moving platform. The resulting scattering data from the 2-dimensional synthetic aperture are used in creating maps of the terrain in front of the platform via a time-reversal technique. We consider several target types, placed on the ground surface or buried, and clutter from rough surfaces with different statistics.					
15. SUBJECT TERMS Computational electromagnetics, hybrid methods, radar imaging, forward-looking radar					
16. SECURITY CLASSIFICATION OF:			17. LIMITATION OF ABSTRACT UU	18. NUMBER OF PAGES 36	19a. NAME OF RESPONSIBLE PERSON Traian Dogaru
a. REPORT Unclassified	b. ABSTRACT Unclassified	c. THIS PAGE Unclassified			19b. TELEPHONE NUMBER (Include area code) (301) 394-1482

Contents

List of Figures	iv
1. Introduction	1
2. Implementation of Equivalent Sources on a Huygens Surface in the NAFDTD Software	2
2.1 Description of the Huygens Surface Approach to Source and Receiver Implementation	2
2.2 Huygens Surface Implementation Details	4
3. Numeric Validation of the Huygens Surface Approach	10
3.1 Huygens Surface Implementation of an Infinitesimal Dipole	10
3.2 Huygens Surface Implementation of a Vivaldi Antenna as Transmitter	12
3.3 Huygens Surface Implementation of a Vivaldi Antenna as Receiver	13
4. Simulation of a Complex Radar Imaging Scenario	16
4.1 Description of the Forward-Looking Radar Imaging System	16
4.2 NAFDTD Simulation of Terrain Mapping by the Forward-Looking Radar	18
5. Conclusions	23
6. References	24
List of Symbols, Abbreviations, and Acronyms	26
Distribution List	27

List of Figures

Fig. 1	Illustration of the EM equivalence principle application to the FDTD algorithm: a) far-field configuration and b) near-field configuration...3
Fig. 2	Vivaldi notch antenna used as the receiver element in the SIRE radar system, showing the a) physical structure and b) computational mesh for EM modeling5
Fig. 3	Near-field transfer function of the Vivaldi notch antenna computed by FEKO at boresight, showing a) magnitude and b) unwrapped phase5
Fig. 4	Illustration of the pulse pre-distortion (channel equalization) procedure employed by the NAFDTD program in the dispersive antenna radiation analysis6
Fig. 5	The 4 th order Rayleigh pulse and its relevant parameters, shown here in the a) time domain and b) frequency domain. The red dotted lines represent the time-domain envelope.7
Fig. 6	Diagram illustrating the simulation scenario involving radiation from an infinitesimal dipole, used in validating the Huygens surface implementation in the NAFDTD program.....11
Fig. 7	Comparison of the results obtained by the analytic and Huygens box NAFDTD implementation of dipole radiation, showing the a) magnitude of E_x component, b) phase of E_x component, c) magnitude of E_z component, and d) phase of E_z component11
Fig. 8	Diagram illustrating the simulation scenario involving the radiation from a Vivaldi notch antenna, used in validating the Huygens surface implementation in the NAFDTD program.....12
Fig. 9	Comparison of the results obtained by direct FEKO and hybrid SIE-FDTD simulations of the Vivaldi antenna near-field radiation, showing the a) magnitude of E_z and b) phase of E_z13
Fig. 10	Diagram illustrating the simulation scenario involving the radiation from an infinitesimal dipole and reception by a Vivaldi notch antenna, used in validating the Huygens surface implementation in the NAFDTD program.....13
Fig. 11	Comparison of the results obtained by direct FEKO and hybrid SIE-FDTD simulations of reception by a Vivaldi antenna, showing the a) magnitude of I_{sc} and b) phase of I_{sc}14
Fig. 12	Schematic representation of the SIRE radar in forward-looking, terrain-mapping mode, showing details of the antenna array mounted on top of the vehicle.....17
Fig. 13	Drawing illustrating the imaging procedure for the FLR, showing the a) side view and b) top view18
Fig. 14	The rough terrain scene containing 11 targets, as modeled by the NAFDTD software.....19

Fig. 15	Illustration of the FLR sensing and imaging areas, as implemented in the NAFDTD software.....	20
Fig. 16	Images of the 20 m by 10 m scene obtained through computer simulations of the FLR, showing a) ground with flat surface; b) ground with randomly rough surface, $h_{rms} = 8$ mm and $l_c = 14.93$ cm; and c) ground with randomly rough surface, $h_{rms} = 16$ mm and $l_c = 14.93$ cm.....	22

INTENTIONALLY LEFT BLANK.

1. Introduction

The software packages based on the finite-difference time-domain (FDTD) method, developed at the US Army Research Laboratory (ARL) since 2001,^{1,2} have been applied to a large variety of radar analysis and performance prediction scenarios. Although by this time they have reached a high degree of maturity and versatility, continuous efforts are being made to enlarge the spectrum of potential applications for this software, with emphasis on scenarios relevant to Army's current research and development programs.

One version of the ARL-developed FDTD software, called NAFDTD, deals with near-field electromagnetic (EM) scattering problems, by which we mean scenarios where the radiation sources and receivers are included inside the computational domain. A previous report² describes revision 1.2 of that software. One shortcoming of that version is that it consisted of a limited selection of source types, approximating the radiation characteristics of very simple antennas. More recent developments have attempted to overcome these limitations by allowing the implementation of arbitrary antennas inside the simulation domain.

Since the classic FDTD algorithm computes the samples of the EM field components on a rectangular grid, direct modeling of arbitrary, non-conformal geometrical shapes that may be part of the antenna design is problematic and can lead to significant errors. In particular, the input impedance and, implicitly, the voltage standing wave ratio (VSWR) are extremely sensitive to the geometry of the antenna feed region—failure to account for the very fine details of this region can lead to gross errors in the evaluation of these critical antenna parameters. Several approaches have been tried in order to mitigate this issue within the FDTD framework: using finer subgrids in the regions containing critical geometrical details; re-casting the FDTD update equations on a grid conformal to a curvilinear coordinate system (e.g., cylindrical); and modifying the FDTD algorithm to accommodate an unstructured grid.³ All these solutions typically lead to a significant increase in the complexity of the FDTD technique, could introduce additional problems (such as numerical instability), and may only address particular antenna geometries. The NAFDTD software does not implement any of these features in the current version and therefore its accuracy for direct antenna analysis cannot be guaranteed at this time.

The indirect approach to antenna implementation described in this report relies on computing the antenna's near-field radiation pattern by an external procedure (using either an analytic, a semi-analytic, or a numeric model), saving that pattern as equivalent currents on a Huygens surface, and using those currents as the

excitation sources in the NAFDTD simulation. A similar procedure can be applied to account for an arbitrary receiving antenna, where the FDTD-computed tangential field components on a Huygens surface can be used as inputs to an antenna analysis model that produces the output voltage or current at its terminals.

After describing the Huygens surface implementation in the NAFDTD code, we perform a validation for some simple problems involving a wideband Vivaldi antenna, both as a transmitter and as a receiver. Then we apply this technique to several complex radar imaging scenarios, based on the forward-looking radar (FLR) geometry. We mention that these FLR simulation scenarios are identical to those published previously,⁴ with the exception that the current work employs more realistic transmitting antennas models as compared to former investigations.

This report is organized as follows. In Section 2, we explain the Huygens surface implementation of the EM radiation sources in the NAFDTD software. Both the basic principles and implementation details are described in this section. In Section 3, we present a numeric validation of these new code features, using a few simple simulations. In Section 4, we apply these ideas to the simulation of a complex radar imaging scenario, involving a FLR geometry, several low-signature targets, and rough surface clutter. We end with conclusions in Section 5.

2. Implementation of Equivalent Sources on a Huygens Surface in the NAFDTD Software

2.1 Description of the Huygens Surface Approach to Source and Receiver Implementation

The application of the EM equivalence principle⁵ in modeling radiation sources and receivers within the FDTD method was described in detail in a previous report.² In this report, we limit ourselves to summarizing the main ideas related to this method.

For our purpose, we apply the equivalence principle as formulated by Love's theorem,⁵ which states that we can replace all the sources (primary and secondary) located inside or outside a closed surface by the tangential field components on that surface, without changing the resulting fields in the complementary region of space. The tangential field components are typically associated with surface current densities \mathbf{J} (electric) and \mathbf{M} (magnetic) according to the equations $\mathbf{J} = \mathbf{n} \times \mathbf{H}$ and $\mathbf{M} = -\mathbf{n} \times \mathbf{E}$, where \mathbf{n} is the normal to the equivalent surface. In antenna radiation analysis, one can replace the physical structure of the antenna with the equivalent current densities created by that antenna on a fictitious closed surface as the new radiation sources. Similarly, when considering the antenna in receiving mode, the

tangential fields that exist in the vicinity of the antenna can be used as equivalent current sources of a wave propagating toward the antenna structure.

As mentioned in a previous report,² the equivalence principle is frequently used in far-field implementations of the FDTD algorithm (where both sources and receivers are removed outside the computational domain), in the implementation of the excitation as a plane wave (via the split-field formulation), as well as in the near-to-far zone transformation.³ Thus, for the excitation implementation, the analytically computed incident fields on the equivalent surface (called here the “Huygens box”) propagate numerically in the inward direction, while in the near-to-far zone transformation, the numerically computed scattered fields on the Huygens box are propagated analytically in the outward direction to the observation point (Fig. 1a). An analog procedure can be applied to the near-field implementation of the FDTD algorithm, where both sources and receivers are placed inside the computational domain (Fig. 1b). In this case, the fields (currents) radiated by the transmitting antenna on the Huygens box are used to excite an outward-propagating wave, while the fields (currents) collected by the receiver Huygens box create an inward-propagating wave that produces a voltage at the antenna terminals.

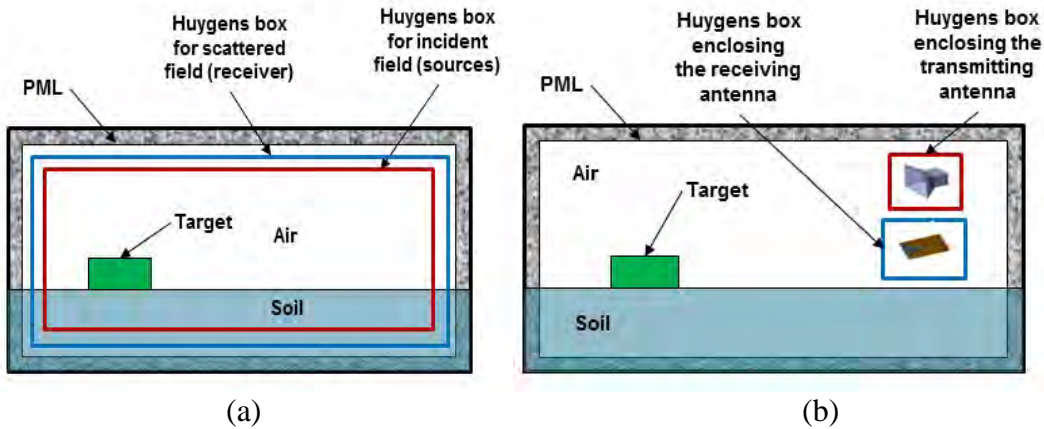


Fig. 1 Illustration of the EM equivalence principle application to the FDTD algorithm: a) far-field configuration and b) near-field configuration

The major challenge with implementing this approach in the near-field FDTD algorithm is the calculation of the equivalent current densities (or tangential field components) along the transmitting antenna Huygens box, and, correspondingly, the computation of the antenna terminal voltage based on the fields present on the receiving antenna Huygens box. Except for very simple cases, the fields in the neighborhood of a radiating antenna cannot be computed exactly via analytical methods. The only general solution to this problem is to perform a separate numerical simulation of the transmitting/receiving antenna by means of a

specialized antenna modeling software. While any computational method of antenna analysis (including FDTD-based ones) can be used for this purpose, in this study we present numerical examples based on the surface integral equation (SIE) solver that comes as part of the FEKO commercial software package.⁶

In the NAFDTD program, the excitation is specified by providing a list of equivalent current components (both \mathbf{J} and \mathbf{M}), at the desired locations and frequencies of interest, stored in the *.currents* input file.² These are computed by the external antenna analysis method (in our case, FEKO), starting with the physical antenna structure and sampling the radiated fields at discrete points on the surrounding Huygens box, corresponding to the field sample locations in the FDTD algorithm. Without going into details, we need to mention that particular attention must be paid to the relative location of the various field components, which are spatially staggered within the FDTD elementary cell.³

The structure of the input files specifying the radiation sources for the NAFDTD software remains largely unchanged as compared to previous versions (more on that in the next section). As a reminder, the *.currents* file contains the list of frequency-domain electric and magnetic current components (or electric/magnetic “dipoles”) at the locations of interest. Notice that the frequency-domain format of the data in the *.currents* file is a good match to the SIE solver output in the FEKO software, which also operates in the frequency domain. The choice of frequency samples for these data points is discussed in Section 2.2.

On the receiver side, the electric and magnetic field components propagating in the vicinity of the antenna are sampled on the surrounding Huygens box and saved in the *.tnear* (time-domain data) and *.fnear* (frequency-domain data) files at frequency points specified in the *.input* file. Importantly, the receiving antenna physical structure is *not* included in the computational domain. These fields are used as excitation in the receiving antenna analysis procedure to obtain the desired quantity at the antenna terminals (which typically is the open-circuit voltage or the short-circuit current). Once again, in this report, we employ the SIE solver within the FEKO software for the numerical analysis of the receiving antenna.

2.2 Huygens Surface Implementation Details

The NAFDTD code implements the excitation waveform as a short, ultra-wideband (UWB) impulse; as such, it closely mimics the operation of an impulse UWB radar. The design of antennas suitable for this type of radar is a challenging issue, requiring both good impedance matching and phase linearity over a wide band of frequencies.⁵ Any departure from these ideal conditions leads to dispersion of the excitation pulse, which is an unwanted effect in imaging radar systems, causing

loss of resolution and multiple replicas of target images. From a numerical standpoint, the pulse dispersion may be unacceptable in an FDTD-based code, which typically requires quiet initial and final field conditions throughout the computational domain.

An example of UWB antenna used in several numerical simulations throughout this report is the Vivaldi notch element, shown in Fig. 2. This particular Vivaldi antenna design, with an operational frequency band from approximately 0.3 to 2.5 GHz, is used by the Synchronous Impulse Reconstruction (SIRE) radar system, which is described in Section 4 of this report. More details on the antenna itself can be found elsewhere.⁷ As shown in Fig. 3, this antenna exhibits both ripples in the magnitude and nonlinearity in the phase of its near-field transfer function (measured as the vertical electric field component closest to the radiating end). (As a side note, we should mention that an antenna can be dispersive in the near-field, even as it is non-dispersive in the far-field; however, only the near-field characteristics are relevant to the NAFDTD simulation scenarios that involve a Huygens surface approach.)

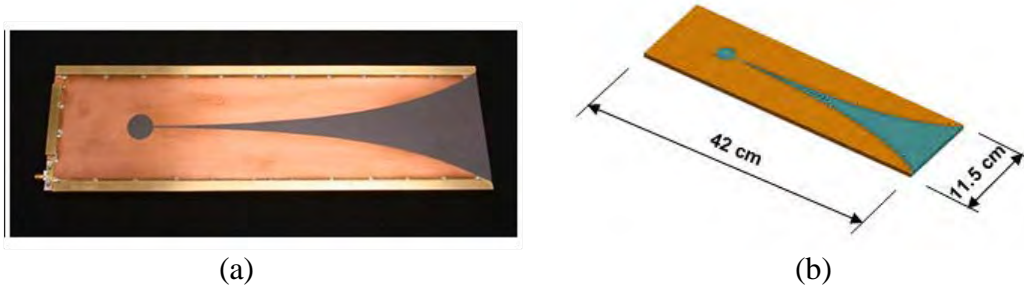


Fig. 2 Vivaldi notch antenna used as the receiver element in the SIRE radar system, showing the a) physical structure and b) computational mesh for EM modeling

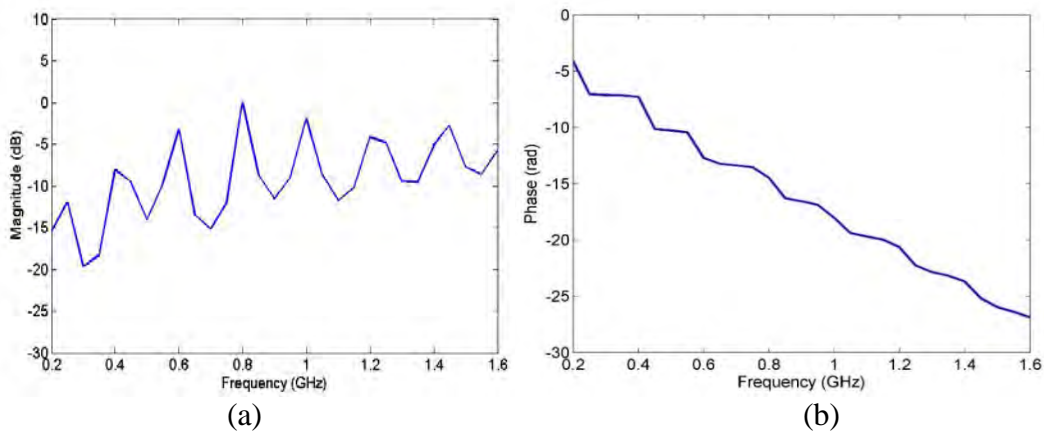


Fig. 3 Near-field transfer function of the Vivaldi notch antenna computed by FEKO at boresight, showing a) magnitude and b) unwrapped phase

Our approach to mitigating this issue consists of using the inverse of the previously mentioned transfer function $A(\omega)$ to compensate for the antenna non-ideal behavior before propagating the excitation waveforms in the time domain. The reverse operation is performed (in the frequency domain) at the radar receiver in order to compute the true target signature that includes the antenna dispersive effects. Importantly, the same equalization transfer function must be used for all current sample locations on the Huygens box; in practice, we found this procedure quite effective, given the high correlation between the transfer functions at all current locations, in both magnitude and phase.

The entire process, illustrated step-by-step in Fig. 4, is performed inside the NAFDTD program and is completely transparent to the user. The effect of this procedure is that the time-domain waveforms used as excitation at the sample points on the Huygens box look very similar to the ideal impulse fed to the antenna terminals. It should be noted that this approach is related to waveform pre-distortion and channel equalization techniques, which are common in many radio frequency (RF) systems, including wireless communications.

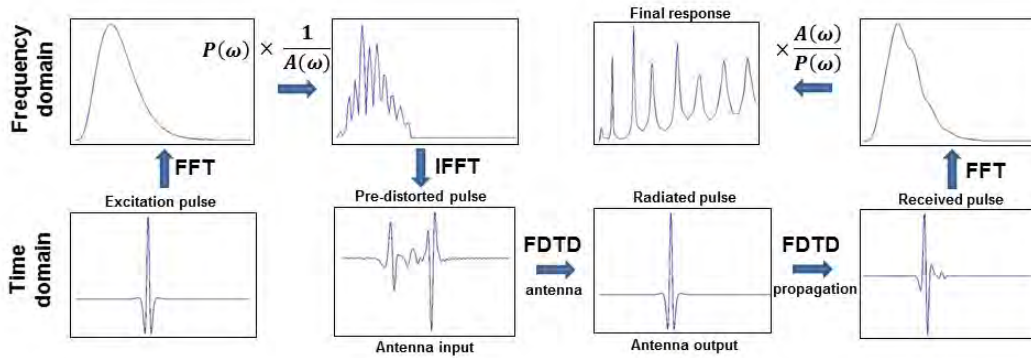


Fig. 4 Illustration of the pulse pre-distortion (channel equalization) procedure employed by the NAFDTD program in the dispersive antenna radiation analysis

Another issue that needs to be discussed here is the choice of frequency data points for the excitation currents produced by the external antenna analysis procedure. Although the FDTD algorithm operates internally with the excitation currents in time-domain format, these currents are stored and provided as program input data in the frequency domain. The conversion from one domain to the other is typically provided by a fast Fourier transform (FFT). The number of frequency data points corresponding to a direct FFT of the time-domain currents used by the FDTD time-marching scheme is very large (equal to the number of time steps required by this process)—implementation of this approach would place a very heavy burden on both the computer time (proportional to the number of frequencies) and storage (the size of the *.currents* file) required for antenna analysis. Fortunately, as shown in

this section, the number of frequency data points for the excitation currents can be reduced significantly without loss in the FDTD solution accuracy. Moreover, this number is independent of most FDTD program parameters, such as frequency band, spatial/temporal sampling rate, and total number of time steps.

The argument for a limited number of frequencies required to reconstruct the excitation impulse is based on 2 observations: 1) the number of non-zero samples of this impulse is typically much smaller than the total number of time steps in the FDTD simulation, therefore the remaining impulse time samples can be filled in by zero-padding in the time domain; and 2) the oversampled time-domain sequence in the FDTD algorithm can be reconstructed from a frequency-domain sequence sampled at the Nyquist rate and zero-padded (in the frequency domain) before taking an inverse FFT. In the actual implementation of the NAFDTD software, the current sources are “turned on” (meaning they are added to the FDTD update equations) for only a limited time interval, denoted by T , while during the rest of the time marching process they are “turned off” (not included in the equations). The quantitative analysis presented here applies primarily to the 4th order Rayleigh pulse,⁸ shown in Fig. 5, and used most frequently as excitation in our FDTD models; however, similar guidelines apply to any other baseband UWB impulses typically employed by FDTD algorithms.

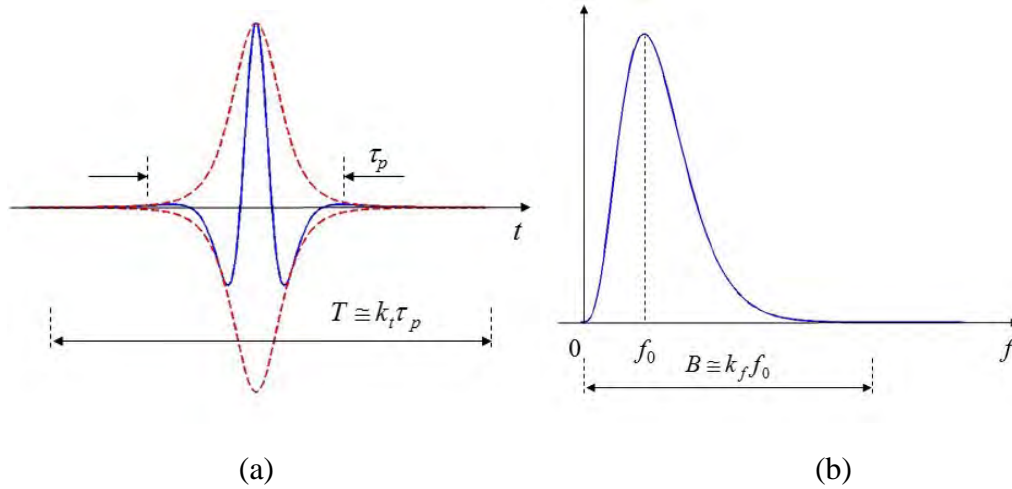


Fig. 5 The 4th order Rayleigh pulse and its relevant parameters, shown here in the a) time domain and b) frequency domain. The red dotted lines represent the time-domain envelope.

Let τ_p the approximate impulse time duration, f_0 the frequency of its spectral peak, and B the bandwidth over which the excitation pulse is computed and stored. For a 4th order Rayleigh pulse, the following approximate relationship holds:

$$\tau_p \cong \frac{2}{f_0}. \quad (1)$$

Now we set $T = k_t \tau_p$ and $B = k_f f_0$, where k_t and k_f are safety factors ensuring that the pulse amplitude goes to zero at the edges of its support in both time and frequency domains. Reasonable choices for these factors are $k_t = 5$ and $k_f = 4$. If the bandwidth B is covered by N_f samples at intervals Δf , then $B = N_f \Delta f$. Assuming the time-domain version of the pulse is obtained from the frequency-domain data by inverse FFT, we have

$$\Delta f = \frac{1}{T} = \frac{1}{k_t \tau_p} \cong \frac{f_0}{2k_t}. \quad (2)$$

From here, we derive that

$$N_f = \frac{B}{\Delta f} \cong 2k_f k_t. \quad (3)$$

For the numerical values previously suggested for k_t and k_f , we obtain $N_f \cong 40$. Clearly, this number is independent of f_0 , as well as the sampling rate of the FDTD algorithm or the total number of time steps. The values of the N_f points on the frequency scale are set from 0 to $(N_f - 1)\Delta f$, at equal intervals Δf given by Eq. 2.

So far, the derivation of N_f did not take into account the pulse propagation delay as it travels from the antenna's feed point (where the time and phase origins are located) to the farthest point on the Huygens box (where the equivalent currents are sampled). Assuming the Huygens box is tightly fit around the antenna structure, this delay is

$$\tau_d \cong \frac{L}{c} = k_p \tau_p \cong k_p \frac{2}{f_0}, \quad (4)$$

where c is the speed of light, L is the antenna's largest dimension, and k_p is an additional factor related to τ_d . From Eq. 4, we derive that

$$k_p \cong \frac{L}{2\lambda_0}, \quad (5)$$

where λ_0 is the wavelength at f_0 . The delay τ_d increases the period of time T for which the current sources must be on; correspondingly, the factor k_t must be increased by adding k_p to it. Notice that this delay becomes significant only for physically long antennas, when $k_p > 1$, or, in other words, the antenna is at least 2

wavelengths long. For most situations, the choice $k_t = 5$ is adequate to cover the pulse propagation delay through the antenna within the time interval T .

Finally, we describe a few minor changes to the input-output file format for the NAFDTD program in the current version (1.4) as compared to version 1.2 described in a previous report.² Thus, in the *.sources* file, the second line, describing the type of current sources, now admits the entries “direct,” “huygens,” or “huygequal” (the last option indicates that pulse equalization takes place inside the FDTD code). In the same file, the third line entry now represents N_f , or the number of frequencies data points stored in the *.currents* file, replacing the time-domain skip factor from version 1.2. All the other entries to the inputs files remain the same as in the old version.

The output of the NAFDTD program consists of the *.tnear* and *.fnear* files.² In the previous version, only 1 set of output files was produced by the program at the end of the run, regardless of the type of EM problem that was analyzed. In version 1.4, modeling a scattering problem produces 2 sets of output files: one contains the total fields, while the other the scattered fields obtained in the simulation. For a project named *projname*, the output files are named *projname_total.tnear/fnear* (for the total field) and *projname_scatter.tnear/fnear* (for the scattered field). If a radiation problem is modeled instead, only the *projname_total.tnear/fnear* set of total field files is produced.

In the current version, both the *.tnear* and *.fnear* files contain the field data obtained directly from the FDTD equations, without attempting to reverse the pre-distortion procedure (or multiply by $A(\omega)$ in the frequency domain) that might have been applied to the excitation sources. However, the *.fnear* file includes, among other data, the complex sequence $A(\omega)$ computed at the output frequency points (which do not have to coincide with the frequency points of the excitation currents). If no pulse pre-distortion is performed during the simulation, then $A(\omega)$ is set to 1. The exact structure of the *.fnear* file (which has a binary format) is the following:

- The sequence of nf_{out} frequencies (in GHz) for the output data.
- The complex values of $A(\omega)$ at each output frequency, stored as real-part/imaginary-part pairs of real numbers.
- The frequency-domain field samples, stored within 3 nested loops, with the frequency index varying first, the field component type varying next, and the grid point index varying last (see the report² on version 1.2 for further explanations). Note that the *.fnear* file structure changed as compared to version 1.2, while the *.tnear* file structure remained the same.

3. Numeric Validation of the Huygens Surface Approach

3.1 Huygens Surface Implementation of an Infinitesimal Dipole

The EM source implementation via the Huygens surface approach in the NAFDTD code can be validated by comparing the results of a simulation using equivalent source excitation with those of a simulation based on direct implementation of exactly the same excitation source. The only real challenge to performing such a comparison is the calculation of the equivalent currents on the Huygens box corresponding to the particular source under consideration. While in most cases the equivalent current computation must be carried out numerically, there is 1 simple case that admits an analytic (closed-form) solution—the infinitesimal dipole. Thus, the electric and magnetic fields produced by an infinitesimal electric dipole with electric current moment \mathbf{I} and arbitrary orientation in free-space are given by⁹

$$\mathbf{E}(\mathbf{r}) = \frac{-jk_0 Z_0 e^{-jk_0 r}}{4\pi r} \left[\mathbf{I} \left(1 - \frac{j}{k_0 r} - \frac{1}{k_0^2 r^2} \right) - \mathbf{u}_r (\mathbf{u}_r \cdot \mathbf{I}) \left(1 - \frac{3j}{k_0 r} - \frac{3}{k_0^2 r^2} \right) \right], \quad (6)$$

$$\mathbf{H}(\mathbf{r}) = -\mathbf{u}_r \times \mathbf{I} \frac{jk_0 e^{-jk_0 r}}{4\pi r} \left(1 - \frac{j}{k_0 r} \right), \quad (7)$$

where \mathbf{r} is the distance vector to the source, r its magnitude, \mathbf{u}_r its direction unit vector, Z_0 is the free-space impedance, and k_0 the free-space wavenumber.

The specific simulation setup for this validation case is described in Fig. 6. In the direct source implementation, the excitation dipole is placed at the coordinate system origin, in vertical orientation and the field probe (receiver) is placed at coordinates (0.32, 0.32, 0.32) (all in meters). The FDTD cell size is 1.6 cm. The results are presented in frequency domain (magnitude and phase), for a frequency range between 50 and 600 MHz. For the Huygens surface excitation, we used a cubic box with 0.16 m on each side, centered in the origin—this involved the computation of 11 spatial samples of the tangential electric and magnetic field (or equivalent surface currents) along the 3 Cartesian directions on each surface of the box. The results for the E_x and E_z components are shown in Fig. 7. The match between the 2 solutions is excellent (within a fraction of 1 dB).

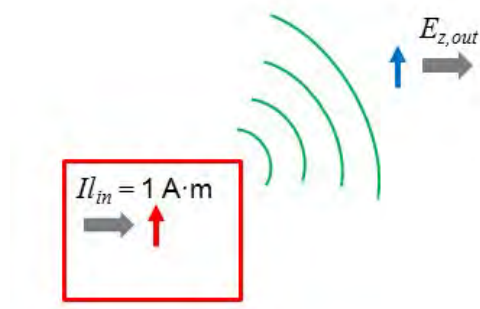


Fig. 6 Diagram illustrating the simulation scenario involving radiation from an infinitesimal dipole, used in validating the Huygens surface implementation in the NAFDTD program

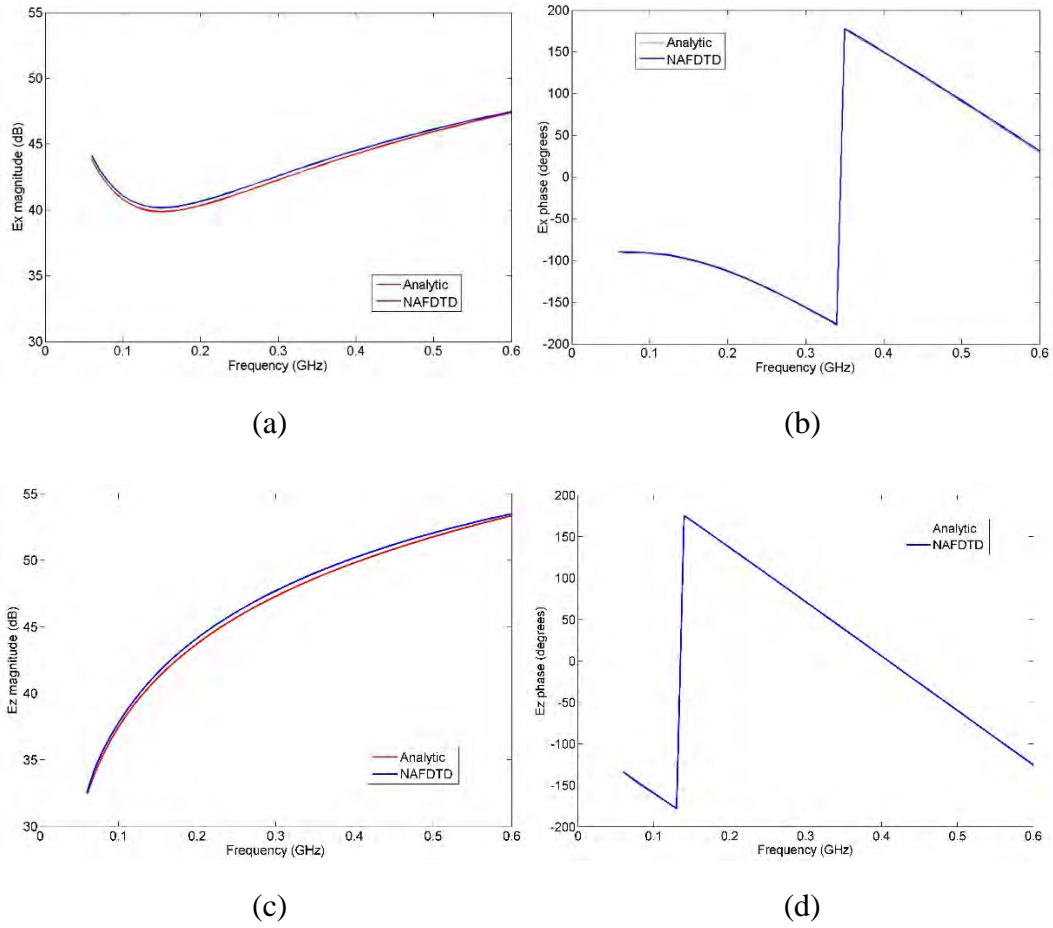


Fig. 7 Comparison of the results obtained by the analytic and Huygens box NAFDTD implementation of dipole radiation, showing the a) magnitude of E_x component, b) phase of E_x component, c) magnitude of E_z component, and d) phase of E_z component

3.2 Huygens Surface Implementation of a Vivaldi Antenna as Transmitter

In this section, we consider a more complex case, where the excitation source is the wideband Vivaldi notch antenna introduced in Section 2.2. The simulation setup is described in Fig. 8. The Huygens box, of dimensions 0.51 by 0.08 by 0.16 m, completely surrounds the antenna. The receiving field probe is placed at coordinates (3, 0, 0) (in meters) with respect to the antenna feed (which coincides with the coordinate system origin). The antenna's radiated near-field under a delta gap excitation voltage of 1 V is computed by FEKO at 40 frequencies equally spaced between 50 MHz and 2 GHz. These frequency samples are sufficient to reconstruct the time-domain near-field on the Huygens box, when the excitation is provided by a 4th order Rayleigh pulse with a spectral peak at 500 MHz. Since the antenna is dispersive, the NAFDTD code applies the pulse pre-distortion procedure described in Section 2.2. The FDTD cell size is 1 cm.



Fig. 8 Diagram illustrating the simulation scenario involving the radiation from a Vivaldi notch antenna, used in validating the Huygens surface implementation in the NAFDTD program

To validate the NAFDTD results for this case, we compare the E_z component at the receiver point as computed by the hybrid procedure outlined in the previous paragraph with a direct FEKO solution of the entire simulation scenario. The comparison is made in the frequency domain (Fig. 9) by plotting both the magnitude and phase over a frequency range between 0.2 and 1.6 GHz. The agreement between the 2 methods is excellent. The slight degradation in the phase accuracy as the frequency increases is caused by numerical dispersion of the FDTD algorithm³ and not by the handling of the antenna implementation.

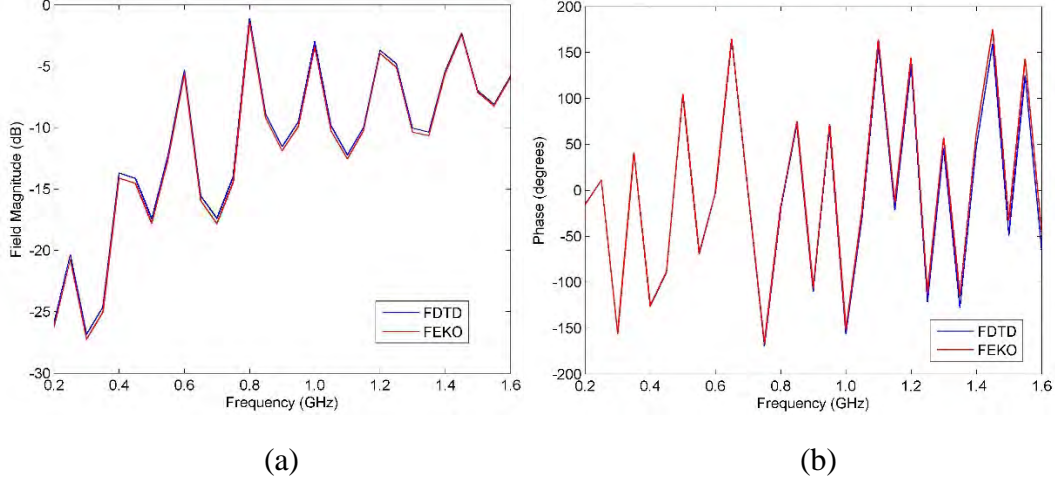


Fig. 9 Comparison of the results obtained by direct FEKO and hybrid SIE-FDTD simulations of the Vivaldi antenna near-field radiation, showing the a) magnitude of E_z and b) phase of E_z

3.3 Huygens Surface Implementation of a Vivaldi Antenna as Receiver

A separate simulation is performed to validate the Huygens surface approach for the receiver antenna implementation. We consider again the same Vivaldi wideband antenna, this time as a receiver, while the radiation source is provided by a vertical infinitesimal dipole with a current moment of 1 A·m. The setup is schematically shown in Fig. 10. The antenna terminals (same as the feed point in the previous section) are placed at coordinates (3, 0, 0) with respect to the dipole (which is located in the origin). The simulation uses the same FDTD cell size, Huygens box size, and frequency range as in Section 3.2.



Fig. 10 Diagram illustrating the simulation scenario involving the radiation from an infinitesimal dipole and reception by a Vivaldi notch antenna, used in validating the Huygens surface implementation in the NAFDTD program

The results are presented in Fig. 11 as magnitude and phase of the frequency-domain, short-circuit current at the antenna terminals. This quantity is computed by 2 methods: one employs NAFDTD to model the radiation and propagation from the dipole to the Huygens box, saves the tangential field components on this box, and then uses these as secondary sources in the FEKO computation of the current at the

antenna terminals; the other uses FEKO to simulate the entire problem. Again, the agreement between the 2 approaches is excellent.

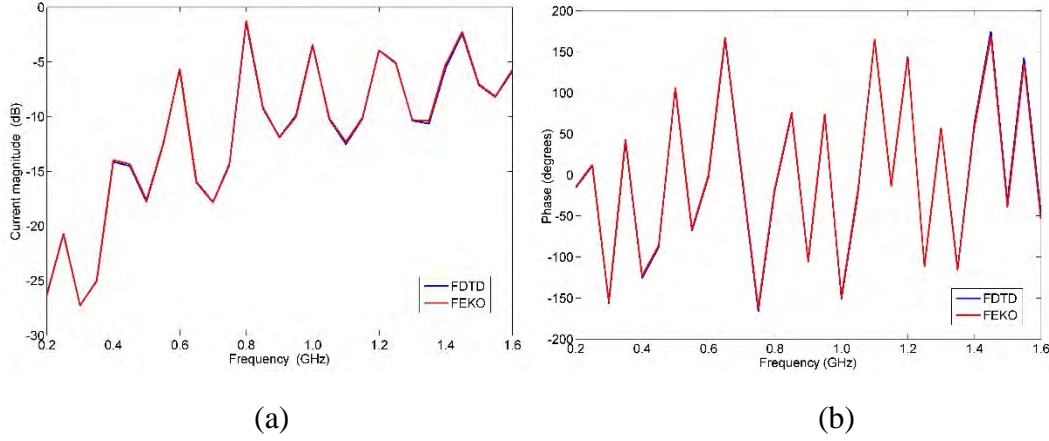


Fig. 11 Comparison of the results obtained by direct FEKO and hybrid SIE-FDTD simulations of reception by a Vivaldi antenna, showing the a) magnitude of I_{sc} and b) phase of I_{sc}

One interesting comment can be made about the graphs in Figs. 9 and 11, which are identical (Fig. 9a with 11a, and 9b with 11b), although the linear-scale units for magnitude differ between the 2 cases. In fact, the connection between the 2 simulations represent a perfect illustration of the reciprocity theorem in electromagnetics.^{5,10} To demonstrate this, we start with the following form of the theorem:

$$\iiint \mathbf{E}_2 \cdot \mathbf{J}_1 dV = \iiint \mathbf{E}_1 \cdot \mathbf{J}_2 dV, \quad (8)$$

where \mathbf{E}_1 is the electric field distribution produced by the electric current sources \mathbf{J}_1 and \mathbf{E}_2 is the electric field distribution produced by the electric current sources \mathbf{J}_2 . The integrals are taken over the entire space. Notice that $\mathbf{E}_{1,2}(x, y, z)$ are fields that extend everywhere in space, whereas $\mathbf{J}_{1,2}(x, y, z)$ are typically localized current distributions associated with EM radiation sources (or transmitting antennas). Because of the current density localization, the integration domains can be restricted to regions surrounding each antenna involved in the transmission-reception scenario.

In our specific case, the 2 antennas under consideration are the Vivaldi (corresponding to the left-hand side of Eq. 8) and the infinitesimal dipole (corresponding to the right-hand side of Eq. 8). Let \mathbf{J}_2 be the current density in the region around the infinitesimal dipole (of moment $I_d l$, located at \mathbf{r}_2 and oriented along the z direction) and \mathbf{E}_1 the fields produced by the Vivaldi antenna in

transmitting mode in the scenario described in Section 3.2. Since $\mathbf{J}_2(\mathbf{r}) = I_d \mathbf{u}_z \delta(\mathbf{r} - \mathbf{r}_2)$, the right-hand side of Eq. 8 can be written as

$$\iiint \mathbf{E}_1 \mathbf{J}_2 dV = \iiint \mathbf{E}_1(\mathbf{r}) I_d \mathbf{u}_z \delta(\mathbf{r} - \mathbf{r}_2) dV = E_{1z}(\mathbf{r}_2) I_d l. \quad (9)$$

For the Vivaldi antenna region (the left-hand side of Eq. 8), we first consider excitation by an ideal (infinite impedance) current generator I_{in} at the antenna terminals in transmitting mode, as well as the open-circuit voltage V_{oc} produced by the infinitesimal dipole when the antenna works in receiving mode. Assuming a delta-gap excitation, the current density across the terminal gap is $\mathbf{J}_1(\mathbf{r}) = I_{in} (\Delta x) \mathbf{u}_g \delta(\mathbf{r} - \mathbf{r}_1)$, where \mathbf{r}_1 is the location of the gap, Δx its length and \mathbf{u}_g the unit vector describing its orientation (this can be arbitrary). At the same time, the electric field across the gap in receiving mode is $\mathbf{E}_2(\mathbf{r}) = \frac{V_{oc}}{\Delta x} \mathbf{u}_g$. When computing the integral in the left-hand side of Eq. 8, only the terminal gap region needs to be taken into account. This is because, although non-zero surface current densities are present on the antenna's metallic parts in transmitting mode, the tangential electric fields on the same parts in receiving mode are zero; therefore, the product $\mathbf{E}_2 \mathbf{J}_1$ is null everywhere except in the terminal gap. Consequently, the left-hand side of Eq. 8 can be written as

$$\iiint \mathbf{E}_2 \mathbf{J}_1 dV = \iiint \mathbf{E}_2(\mathbf{r}) I_{in} (\Delta x) \mathbf{u}_g \delta(\mathbf{r} - \mathbf{r}_1) dV = \mathbf{E}_2(\mathbf{r}_1) I_{in} (\Delta x) \mathbf{u}_g = V_{oc} I_{in}. \quad (10)$$

Additionally, we use a well-known result in antenna theory that relates the excitation voltage V_{in} (of an ideal voltage generator of zero impedance) and current I_{in} at the antenna terminals to the open-circuit voltage V_{oc} and short-circuit current I_{sc} at the same terminals in receiving mode:¹⁰

$$\frac{V_{in}}{I_{in}} = \frac{V_{oc}}{I_{sc}} = Z_A, \quad (11)$$

where Z_A is the antenna's input impedance. Combining all previous equations yields the following result:

$$V_{oc} I_{in} = V_{in} I_{sc} = E_{1z}(\mathbf{r}_2) I_d l. \quad (12)$$

Now focusing on the second part of this identity, if we make $V_{in} = 1$ V and $I_d l = 1$ A·m (as in the last 2 section's simulations), we obtain $I_{sc} = E_{1z}(\mathbf{r}_2)$, which is the result we were after (notice again that the units are different in the 2 sides of this identity). Alternatively, we could use a current excitation $I_{in} = 1$ A for the Vivaldi antenna in transmitting mode and measure the open-circuit voltage at its

terminals in receiving mode. In that case, we would obtain $V_{oc} = E_{1z}(\mathbf{r}_2)$, with the appropriate units on each side.

4. Simulation of a Complex Radar Imaging Scenario

4.1 Description of the Forward-Looking Radar Imaging System

After validating the Huygens surface approach to antenna implementation in the NAFDTD software, we apply the method to a complex radar imaging scenario, simulating the operation of the SIRE FLR. This system was designed and built at ARL as an experimental UWB radar testbed for applications such as terrain mapping, in-road threat detection, autonomous navigation, and through the wall sensing.¹¹ In this section, we provide a short description of the radar parameters and operational principles, as well as the imaging geometry relevant to the scenario investigated in this report.

SIRE is a vehicle-borne radar system, equipped with a 2-m-wide antenna array comprising 2 transmitting and 16 receiving elements, mounted on top of the vehicle at a height of approximately 2 m. When operating in forward-looking mode, the sensing area is in front of the vehicle, which moves forward, as illustrated in Fig. 12. The transmit antennas are transversal electromagnetic (TEM) horns, placed at the ends of the array, while the receive elements are Vivaldi notch antennas, placed in a uniform linear array along the 2-m aperture (notice that this is the same antenna element used in the models in the previous sections). The transmitter generates short impulses with a 1-ns duration, a pulse repetition frequency (PRF) of 1 MHz, and a frequency band from 300 to 2500 MHz. The average transmitted power is 5 mW.

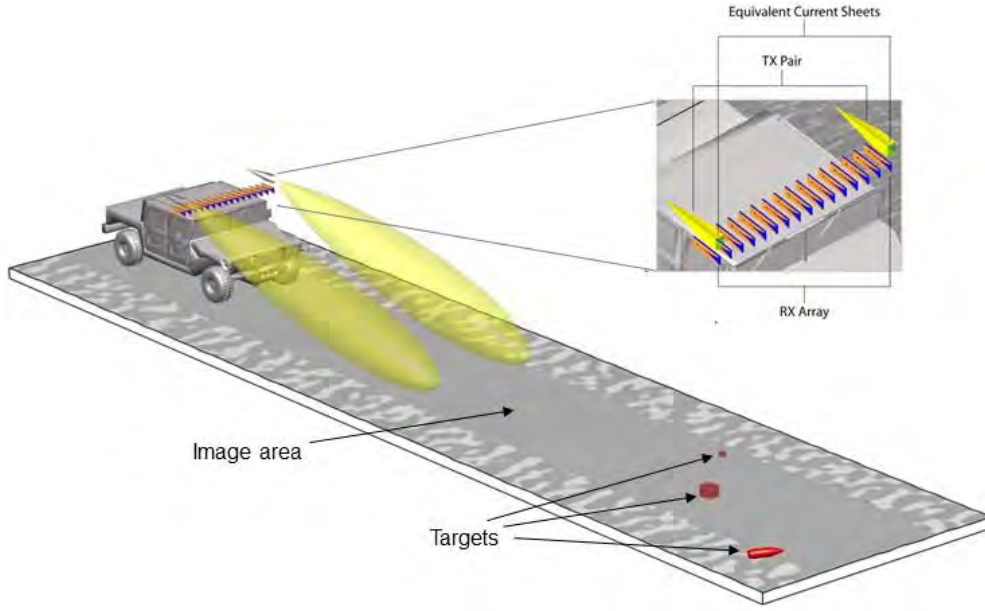


Fig. 12 Schematic representation of the SIRE radar in forward-looking, terrain-mapping mode, showing details of the antenna array mounted on top of the vehicle

The 2 transmitter antennas are activated in an alternating manner with each pulse, while the waves reflected by the scene are simultaneously collected by all Vivaldi elements, each of them connected to a separate receiver channel. In this sense, the SIRE radar can be characterized as a multiple-input, multiple-output (MIMO) system, with the input channel orthogonality implemented by time-domain multiplexing. This MIMO antenna array configuration provides a resolution equivalent to a filled monostatic array of transmitter-receiver pairs that spans the same aperture width. Notice that the array is located at slightly different ranges at the moments when the left and right transmitters are activated, depending on the vehicle speed. The receiver channels use an equivalent sampling scheme and pulse averaging, resulting in an effective PRF (as presented to the image formation algorithm) of about 3 Hz.

The imaging method is mainly based on the backprojection algorithm.¹² However, unlike in a classic side-looking synthetic aperture radar (SAR) geometry, where each image pixel is based on coherently integrating the contributions from along-track positions of the radar, in the forward-looking geometry, one integrates the contributions from all 16 receiver channels at successive ranges as the platforms moves forward. The principle of FLR image formation is described in Fig. 13. Thus, an image pixel (assumed to be situated in the ground plane) is computed based on all receiver data obtained by the radar platform at ranges between R_{min} and R_{max} (these are typically 8 and 33 m, respectively). The down-range image resolution is about 10 cm (dictated by the pulse bandwidth), whereas the cross-range resolution

is about 1 m (dictated primarily by the physical antenna array width). The main advantage of forward-looking, physical-aperture imaging from a moving platform, with a constant average distance from the pixel to the antenna array, over imaging from a fixed platform is that, in the first case, the cross-range resolution is the same for any along-track range, whereas in the second case, this resolution degrades with increasing range. Notice that the image cross-range extent is typically larger than the physical aperture width, therefore, the cross-range resolution degrades for pixels at the edges of the imaging area (which are squinted with respect to the boresight direction) as compared to those in the middle (Fig. 13b).

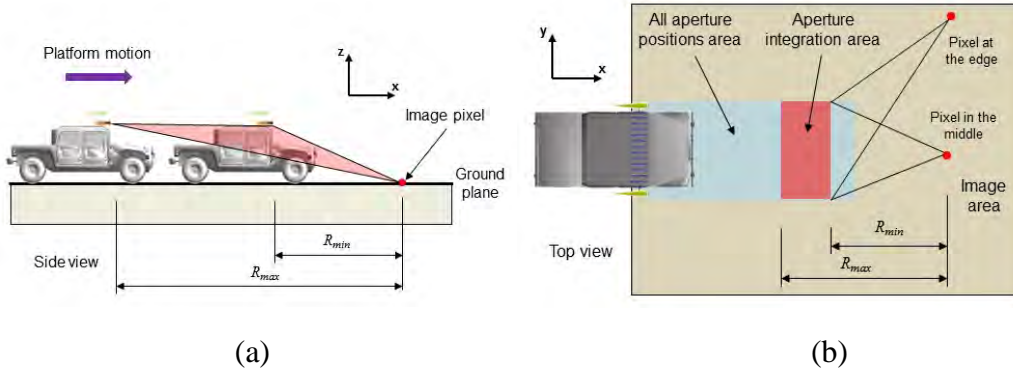


Fig. 13 Drawing illustrating the imaging procedure for the FLR, showing the a) side view and b) top view

4.2 NAFDTD Simulation of Terrain Mapping by the Forward-Looking Radar

In this section, we demonstrate the imaging of a complex scenario based on NAFDTD simulated data that closely mimics the operation of the SIRE radar. In this report, we use the same scene (terrain and targets) and radar sensing geometry as in a previous study.⁴ The only difference between the 2 models is that here we use a full model of the transmitting antenna (implemented via the Huygens surface approach), while in the previous study⁴ we used an approximate equivalent aperture current approach. More specifically, in this study, the transmitters are equipped with the same Vivaldi antennas as described in the Sections 2 and 3.

The Huygens surface approach was not attempted in the receiving antenna implementation, because the computational complexity made it impractical for this type of problem. Thus, the equivalent currents generated by the transmitting antenna on the Huygens box need only be computed once, regardless of the antenna position in space. However, since the fields on the receiving Huygens box change with the antenna position, the receiver antenna model must be run separately for each individual element position during the data collection. Since the receiver

antenna modeling is a tedious and time-consuming process, we decided to avoid this approach. Instead, the receiver data are based on the vertical or horizontal electric field component sampled at the locations of the receiving element feed points.

The scene to be mapped includes a rough ground surface and a collection of 11 targets, buried or placed on-surface, as shown in Fig. 14. The complete list of targets is as follows: 1) buried metallic anti-personnel landmine; 2) buried plastic ($\epsilon_r = 3.1$, $\sigma_d = 2$ mS/m) anti-personnel landmine; 3) on-surface plastic ($\epsilon_r = 3.1$, $\sigma_d = 2$ mS/m) anti-personnel landmine; 4) buried metallic 155-mm shell; 5) buried metallic anti-tank landmine; 6). on-surface metallic anti-tank landmine; 7) buried metallic 155-mm shell; 8) buried metallic 155-mm shell; 9) on-surface metallic anti-personnel landmine; 10) buried plastic ($\epsilon_r = 3.1$, $\sigma_d = 2$ mS/m) anti-tank landmine; and 11) on-surface plastic ($\epsilon_r = 3.1$, $\sigma_d = 2$ mS/m) anti-tank landmine. The ground is assumed to be a homogeneous dielectric medium with $\epsilon_r = 6$ and $\sigma_d = 10$ mS/m (these parameters are considered independent of frequency). In the cases where we study the impact of ground clutter, the rough surface is described by a 2-dimensional random process with Gaussian statistics, characterized by its *rms* height (h_{rms}) and correlation length (l_c). The surface generation algorithm follows a previously described procedure¹³ (more details can also be found in our previous report⁴).

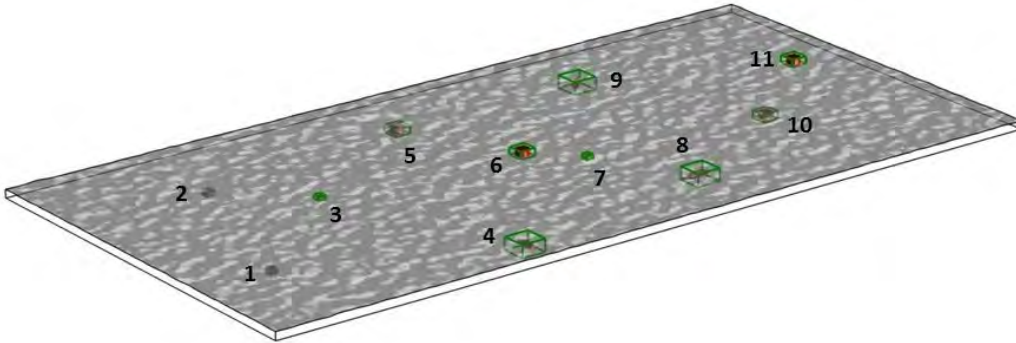


Fig. 14 The rough terrain scene containing 11 targets, as modeled by the NAFDTD software

Figure 15 illustrates the sensing and imaging geometry as implemented in the computer model. The entire terrain area has an extent of about 40 m by 10 m, with the radar platform moving along a 2-m-wide strip of 30-m length. The image area (which contains all the targets) is 20 m by 10 m, placed ahead of the driving range and compatible with the imaging technique described in the previous section. For the simulation, we chose $R_{min} = 10$ m and $R_{max} = 20$ m. The scattering problem is solved numerically frame-by-frame as the vehicle moves forward, with the 2 transmitters firing sequentially and all receivers collecting data simultaneously

during each frame. We considered a total of 90 successive antenna array positions (or “frames”), spaced at 0.333-m intervals apart in down-range (that gives a displacement of 0.666 m between 2 consecutive firings of the same transmitter). The frequency band was restricted to 0.3–1.5 GHz, in 3-MHz increments. The resulting image resolution is approximately 12.5 cm in down-range and 1.25 m in cross-range (see our previous report⁴ for a more rigorous derivation of the imaging system point spread function).

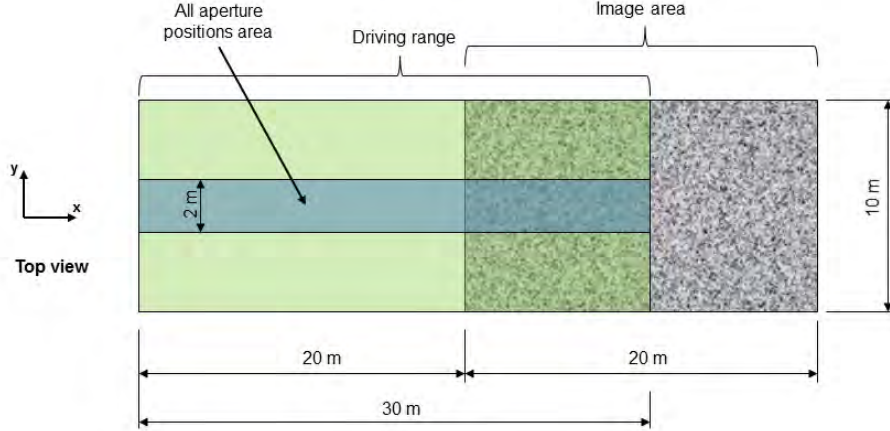


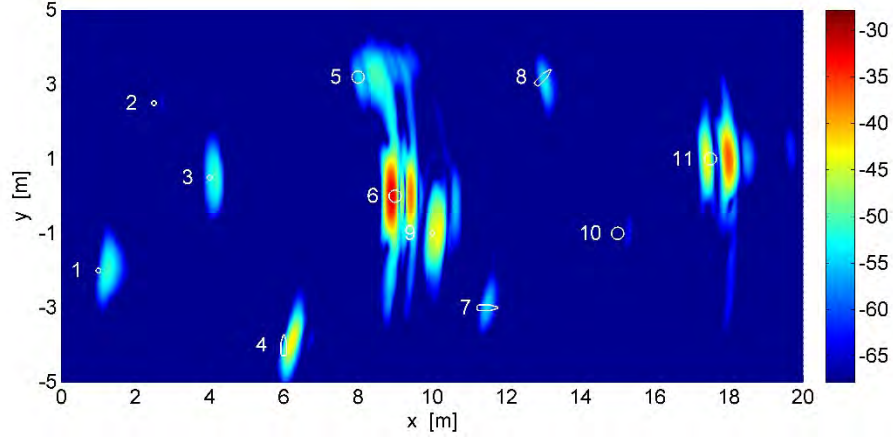
Fig. 15 Illustration of the FLR sensing and imaging areas, as implemented in the NAFDTD software

The radar images were obtained via the time-reversal method (TRM).^{14,15} This algorithm is very similar to the matched filter technique (as applied to SAR imaging,¹⁶) with the exception that, in the TRM, the EM wave propagation is more rigorously accounted for by the Green’s functions that characterize the environment. In our implementation, which follows a previously described method,¹⁷ the half-space Green’s functions were computed using 2nd order asymptotics in order to avoid the time-consuming evaluation of the Sommerfeld integral.¹⁸

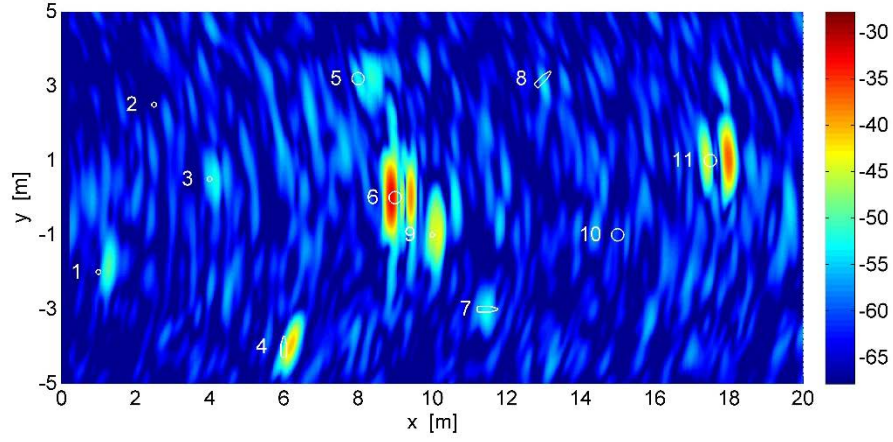
One important aspect of the radar images presented in this section is that, since the transmitting antenna is dispersive, the channel equalization procedure described in Section 2.2 was applied to the excitation pulses before running the NAFDTD simulations. However, at the receivers, we did not multiply the frequency-domain results back with the antenna transfer function (as we did in the example in Section 3.2). If we did so, the presence of multiple echoes from each target and clutter item would produce a very poor image quality. The procedure applied here is in fact a plausible model of a real-life impulse UWB radar system, which operates with dispersive antennas, where pulse pre-distortion is a desired feature to insure a linear-phase response from the scene under interrogation.

Since this simulation involved a very large computational space, it is interesting to discuss the computer resources used by this study. The FDTD grid, with a cell size of 8 mm, was comprised of 4.7 billion cells. The simulations were run on several high performance computing (HPC) platforms at ARL¹⁹ and Air Force Research Laboratory (AFRL)²⁰ Defense Supercomputing Resource Centers (DSRC), using 256 cores for each individual radar position and ground/target scenario. The total runtime necessary to obtain one of the images shown in this section was approximately 400,000 central processing unit (CPU) hours.

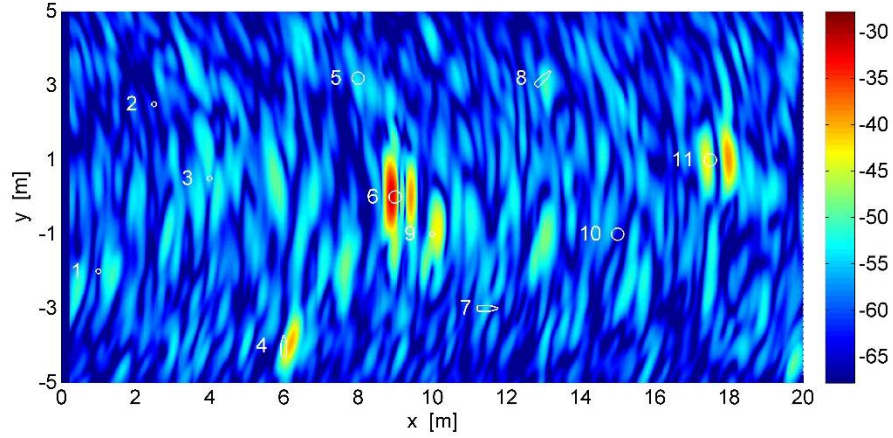
The simulation results for vertical-vertical (V-V) polarization are shown in Fig. 16, for 3 scenarios: a) flat ground surface, b) small ground roughness with $h_{rms} = 8$ mm and $l_c = 14.93$ cm, and c) large ground roughness with $h_{rms} = 16$ mm and $l_c = 14.93$ cm. The results are very similar to those previously reported,⁴ showing that the approximate antenna models considered in that study provide very similar patterns with the Vivaldi antennas employed here. Although the primary purpose of this study was to validate the simulation process rather than analyzing the radar phenomenology, the images in Fig. 16 suggest that the large, on-surface targets can be easily detected even in relatively severe ground clutter; however, the small and/or buried targets are very difficult to detect by this sensor, even in benign ground clutter conditions.



(a)



(b)



(c)

Fig. 16 Images of the 20 m by 10 m scene obtained through computer simulations of the FLR, showing a) ground with flat surface; b) ground with randomly rough surface, $h_{rms} = 8$ mm and $l_c = 14.93$ cm; and c) ground with randomly rough surface, $h_{rms} = 16$ mm and $l_c = 14.93$ cm

5. Conclusions

In this report, we described the implementation of the radar antennas in the NAFDTD software via an equivalence principle approach. The antenna is analyzed by an external procedure (in this work, performed by the SIE solver in FEKO) and connected to the FDTD model by a Huygens surface. The report discussed many of the details involved in this process. Particularly, we explained how to apply the method to UWB radar simulations involving dispersive antennas, using a channel equalization procedure. After validating the technique for several simple scenarios, we applied it to a complex, large-scale sensing scenario, involving FLR imaging of multiple targets in rough surface clutter. The examples in Section 3 proved the excellent accuracy of the Huygens box approach to the antenna implementation. Furthermore, the FLR simulations presented in Section 4 confirmed the validity of our hybrid antenna model.

Efforts are underway to introduce direct antenna implementation in the NAFDTD software, meaning that the entire antenna physical structure would be part of the simulation domain, without the need of performing external analysis and applying the equivalence principle. In fact, the FDTD method has been successfully employed in the past in direct antenna modeling by many investigators.³ However, a major issue with this FDTD application is the accuracy of the spatial discretization, particularly in critical areas of the antenna, such as the feed. A typical approach to these scenarios is to employ very small FDTD discretization cells in the critical areas. Since the NAFDTD implementation features constant cell size throughout the entire computational domain, modeling very large radar scattering problems with these very fine and uniform discretization cells becomes impractical. In fact, this was one of the primary reasons for developing the Huygens surface approach in the first place. As a synthesis of all these ideas, we could envision a future FDTD-FDTD hybrid implementation, where the antenna analysis is performed on a fine FDTD grid, the scattering problem is solved by the same technique on a coarser grid, while a Huygens surface provides the connection between the two.

6. References

1. Dogaru T. AFDTD user's manual. Adelphi (MD): Army Research Laboratory (US); March 2010. Report No.: ARL-TR-5145.
2. Dogaru T. NAFDTD – A near-field finite difference time domain solver. Adelphi (MD): Army Research Laboratory (US); September 2012. Report No.: ARL-TR-6110.
3. Taflove A, Hagness S. Computational electrodynamics: The finite-difference time-domain method. Norwood (MA): Artech; 2000.
4. Liao D, Dogaru T, Sullivan A. Large-scale, full-wave-based emulation of step-frequency forward-looking radar imaging in rough terrain environments. *Sensing and Imaging: An International Journal*. April 2014;15.
5. Balanis C. Antenna Theory – Analysis and design. New York (NY): Wiley; 1997.
6. FEKO EM Simulation Software Web page. <http://www.feko.info> (accessed October 2014).
7. Smith GD, Harris RW, Ressler M, Stanton B. Wideband Vivaldi notch antenna design for UWB SIRE VHF/UHF radar. Adelphi (MD): Army Research Laboratory (US); November 2006. Report No.: ARL-TR-4409.
8. Hubral P, Tygel, M. Analysis of the Rayleigh pulse. *Geophysics*. 1989;54:654–658.
9. Kong JA. Electromagnetic wave theory. Cambridge (MA): EMW Publishing; 2000.
10. Stutzman WL, Thiele GA. Antenna theory and design. New York (NY): Wiley; 1998.
11. Ressler M, Nguyen L, Koenig F, Wong D, Smith G. The ARL synchronous impulse reconstruction (SIRE) forward-looking radar. *Proc. SPIE*. May 2007;6561.
12. Soumek, M. Synthetic Aperture Radar Signal Processing. New York (NY): Wiley; 1999.
13. Thorsos EI. The validity of the Kirchhoff approximation for rough surface scattering using a gaussian roughness spectrum. *The Journal of the Acoustical Society of America*. 1988;83:78–92.

14. Fin, M. Time reversal of ultrasonic fields – Part I: basic principles. IEEE Transactions on Ultrasonics, Ferroelectrics and Frequency Control. September 1992;39(5):555–566.
15. Borcea L, Papanicolaou G, Tsogka C. A resolution study for imaging and time reversal in random media. Contemporary Mathematics. 2003;313:63–67.
16. Richards M, Scheer J, Holm W. Principles of modern radar. Raleigh: SciTech Publishing; 2010.
17. Sarabandi K, Koh I, Casciato M. Demonstration of time reversal methods in a multi-path environment Proceedings of the IEEE Antennas and Propagation Symposium 2004.
18. Liao D, Sarabandi K. Near-earth wave propagation characteristics of electric dipole in presence of vegetation or snow layer. IEEE Transaction on Antennas and Propagation. November 2005;53:3747–3756.
19. ARL DSRC Web page. <http://www.arl.hpc.mil> (accessed April 2015).
20. AFRL DSRC Web page. <http://www.afrl.hpc.mil> (accessed April 2015).

List of Symbols, Abbreviations, and Acronyms

AFRL	US Air Force Research Laboratory
ARL	US Army Research Laboratory
CPU	central processing unit
DSRC	Defense Supercomputing Resource Center
EM	electromagnetic
FDTD	Finite Difference Time Domain
FFT	fast Fourier transform
FLR	forward-looking radar
HPC	High Performance Computing
MIMO	multiple-input multiple-output
PRF	pulse repetition frequency
RF	radio frequency
SAR	synthetic aperture radar
SIE	surface integral equation
SIRE	Synchronous Impulse Reconstruction
TEM	transversal electromagnetic
TRM	time-reversal method
UWB	ultra-wideband
VSWR	voltage standing wave ratio
V-V	vertical-vertical

1 DEFENSE TECH INFO CTR
(PDF) ATTN DTIC OCA

2 US ARMY RSRCH LAB
(PDF) ATTN IMAL HRA MAIL & RECORDS MGMT
ATTN RDRL CIO LL TECHL LIB

1 GOVT PRNTG OFC
(PDF) ATTN A MALHOTRA

5 US ARMY RSRCH LAB
(PDF) ATTN RDRL SER U A SULLIVAN
ATTN RDRL SER U C KENYON
ATTN RDRL SER U C LE
ATTN RDRL SER U D LIAO
ATTN RDRL SER U T DOGARU

INTENTIONALLY LEFT BLANK.